Ultrasensitive Magnetoelectric Sensing System for Pico-Tesla MagnetoMyoGraphy

Siming Zuo, *Student Member, IEEE*, Julius Schmalz, Mesut-Ömür Özden, Martina Gerken, *Member, IEEE*, Jingxiang Su, *Student Member, IEEE*, Florian Niekiel, Fabian Lofink, Kianoush Nazarpour, *Senior Member, IEEE*, and Hadi Heidari, *Senior Member, IEEE*

***Abstract*—Magnetomyography (MMG) with superconducting quantum interference devices (SQUIDs) enabled the measurement of very weak magnetic fields (femto to pico Tesla) generated from the human skeletal muscles during contraction. However, SQUIDs are bulky, costly, and require working in a temperature-controlled environment, limiting wide-spread clinical use. We introduce a low-profile magnetoelectric (ME) sensor with analog frontend circuitry that has sensitivity to measure pico-Tesla MMG signals at room temperature. It comprises magnetostrictive and piezoelectric materials, FeCoSiB/AlN. Accurate device modelling and simulation are presented to predict device fabrication process comprehensively using the finite element method (FEM) in *COMSOL Multiphysics*. The fabricated ME chip with its readout circuit was characterized under a dynamic geomagnetic field cancellation technique. The ME sensor experiment validate a very linear response with high sensitivities of up to 378 V/T driven at a resonance frequency of $f_{\mathrm{res}} = 7.76$ kHz. Measurements show the sensor limit of detections of down to 175 pT/$\sqrt{\mathrm{Hz}}$ at resonance, which is in the range of MMG signals. Such a small-scale sensor has the potential to monitor chronic movement disorders and improve the end-user acceptance of human–machine interfaces.**

***Index Terms*—Biomagnetic field, magnetomyography, magnetoelectric effect, piezoelectric.**

I. Introduction

THE measurement of the electrical activity of the skeletal muscles, that is the electromyography (EMG) technique, is an established method in research and diagnosis of medical conditions [1]. However, the magnetic counterpart of the EMG signal, that is the magnetomyography (MMG) signal, has received less attention since its discovery in 1972 [2]. They defined the MMG method as the recording of one component of the magnetic field vector versus time that is generated by the electric currents that travel along with the skeletal muscles. Therefore, the correspondence between the MMG and EMG methods is governed by the Maxwell-Ampère law. The MMG signals have the potential to offer significantly higher spatial resolution than the EMG signals, while offering the same temporal resolution [3]. In addition, the MMG signal offers a vector information of the activity, higher signal-to-noise, and better positioning and fast screening of sensors without electrical contacts [4]. State-of-the-art clinical EMG recording are even using needle recording probes to accurately assess muscle activity. However the process is painful and limited to tiny areas with poor spatial sampling points [5]. Magnetic sensors with fully biocompatible materials can be fully packaged to form a miniaturized implantable system that could be an efficient and robust alternative to medical diagnosis, rehabilitation, health monitoring, and robotics control [6].

The magnitude of EMG signals is in the scale of milli-volts, however the MMG signal is in the range of femto (10^{-15}) to pico (10^{-12}) Tesla [4], inversely proportional to the distance between the measurement point and the skeletal muscle. In the seminal work of Cohen and Gilver in 1972, they discovered and recorded MMG signals using superconducting quantum interference devices (SQUIDs) [2]. The state-of-the-art MMG measurement by SQUIDs is presented in [7]. Nonetheless, their ultra-high cost and cumbersome weight limit the wide adoption of this magnetic sensing technique within and beyond clinical environment. Optically pumped magnetometers (OPMs) have rapidly developed to enable the study evoked MMG activity which typically enjoy a large signal to noise ratio [8]–[10]. Note that the MMG signal can be easily affected by the magnetic noise, e.g. the magnetic field of the Earth.

Current experiments based on SQUIDs and OPMs for MMG sensing are conducted in heavily-shielded environment, which is expensive and bulky. To enable more wide-spread clinical use and use as a future wearable technology, there is a need for a miniaturized, low-cost and self-powered magnetic sensor that works at a normal (uncooled) temperature. Fig. 1 illustrates magnetic signals produced by various sources from human body

Manuscript received March 15, 2020; revised May 4, 2020; accepted May 20, 2020. Date of publication May 28, 2020; date of current version October 15, 2020. This work was supported under Grants EP/R511705/1, EP/N023080/1, and EP/R004242/1 from EPSRC, U.K. This paper was recommended by Associate Editor Prof. S.-Y. Lee. *(Corresponding author: Hadi Heidari.)*

Siming Zuo and Hadi Heidari are with the Microelectronics Lab James Watt School of Engineering, University of Glasgow G12 8QQ Glasgow, U.K. (e-mail: z.siming.1@research.gla.ac.uk; hadi.heidari@glasgow.ac.uk).

Julius Schmalz, Mesut-Ömür Özden, and Martina Gerken are with the Institute of Electrical Engineering and Information Technology, Christian-Albrechts-University of Kiel, Kaiserstraße 2 24143, Kiel, Germany (e-mail: jusc@tf.uni-kiel.de; omoz@tf.uni-kiel.de; mge@tf.uni-kiel.de).

Jingxiang Su, Florian Niekiel, and Fabian Lofink are with the Fraunhofer Institute for Silicon Technology ISIT, 25524 Itzehoe, Germany (e-mail: jingxiang.su@isit.fraunhofer.de; florian.niekiel@isit.fraunhofer.de; fabian.lofink@isit.fraunhofer.de).

Kianoush Nazarpour is with the School of Engineering and the Biosciences Research Institute, Newcastle University, NE1 7RU Newcastle upon Tyne, U.K. (e-mail: kianoush.nazarpour@newcastle.ac.uk).

This article has supplementary downloadable material available at https://ieeexplore.ieee.org, provided by the authors.

Color versions of one or more of the figures in this article are available online at https://ieeexplore.ieee.org.

Digital Object Identifier 10.1109/TBCAS.2020.2998290

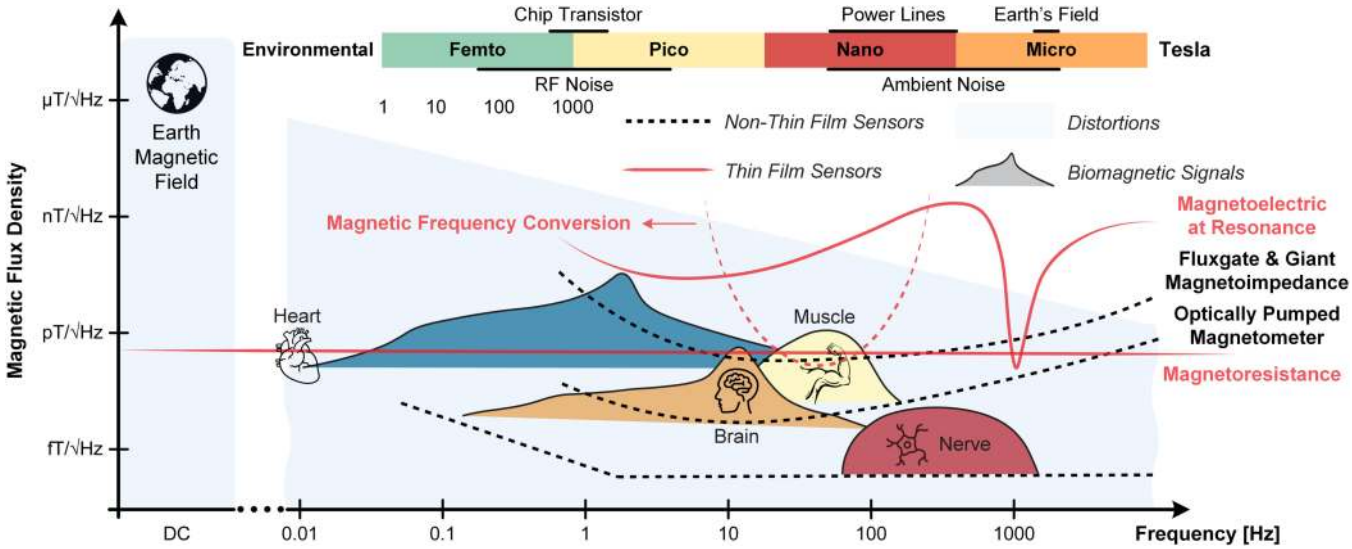

Fig. 1. Comparison of amplitude densities of magnetic signals generated by various sources of the human body, with LODs of different magnetic sensor types.

with emergence of efficient magnetic technologies [6], [11]. The magnitude of the MMG signals is lower than that of the heart [4]. The minimum spectral density could reach limit of detection (LOD) of hundreds of fT/$\sqrt{}$Hz, which depends on muscle to sensor distance and appeared in the typical frequency range from 10 Hz and 100 Hz. The magnitude of the MMG signal varies with the third power of the distance between the transducer and muscle fiber. Significant dimensional changes of the skeletal muscle during contraction or a human movement or the body part under investigation, thus, can affect the quality of the MMG signal. In all the human studies the MMG signals were recorded during isometric contractions; where the length of the muscles does not change despite the force it generates.

The current standard method performing the MMG measurement is the SQUID, which has a limit-of-detection about sub-fT/$\sqrt{}$Hz range. However, it is bulky, expensive, energy consumptive because of the required cooling and large shielding environment. The OPMs with small physical size have been improved significantly in their LODs during recent years, especially from competing manufacturers e.g. QuSpin Inc., FieldLine Inc. and Twinleaf. A below 100 fT/$\sqrt{}$Hz sensitivity has been achieved [12], [13]. Unfortunately, the process of setting up OPMS sensors is rather complex and the sensors is still expensive. Fluxgate sensors and giant magnetoimpedance (GMIs) sensors are well-established sensor concepts and both have similar dimensions, frequency ranges and LODs at low pT/$\sqrt{}$Hz ranges [14], [15]. Despite that they are very small, their LOD is not as good as that of OPMs and SQUIDs, rendering them unsuitable for MMG sensing.

Thin-film magnetoelectric (ME) sensors have increasingly drawn attention due to their small dimensions and the possibility of integration with micro-electromechanical systems [16], [17]. Currently, self-organized ME sensors are promising candidates as magnetic field sensors operating at room temperature [18], [19]. The ME sensors offer passive detection, high sensitivity, large effect enhancement at mechanical resonances, and large linear dynamic range. This type of sensors recently have achieved a high pT/$\sqrt{}$Hz LOD range at low frequencies [20]–[22]. Additionally, the LODs at a mechanical resonance state are already lower than fluxgate sensors and GMIs [23]. To measure low-frequency magnetic signals, magnetic frequency conversion techniques (MFCs) with modulation coils should be implemented, to enable measurement at virtually any frequency outside the mechanical resonance. The noise performance over a frequency range of 100 Hz can be interpreted as the LOD as a function of frequency. The resonance curve of the sensor is compensated by digital equalization. The MFCs for ME sensors has been explained in detail in [21]. Recently, they have been successfully used in magnetocardiography measurement with a volunteer inside a magnetically shielded room to remove the large unwanted magnetic background noise [20]. Although their sensitivities are not as high as that of the SQUIDs, the ME sensors show significant superiority in simple preparation and low cost. Furthermore, the ME sensors are CMOS compatible [16], [24] and have a lower LOD compared to other integrated semiconductor magnetic sensors. We developed a high-performance Hall sensor integrated with its readout circuit in CMOS technology previously [25]. However, Hall sensors require a highly stable DC power supply to excite the Hall effect and a complex interface circuit to process collected weak Hall voltages under surrounding noise [26]. Spintronic sensors [27], particularly our previous design of tunnel magnetoresistance (TMR) sensors [28], offer high sensitivity and small size for biosensing applications. However, both a single TMR sensor and a sensor array (Wheatstone bridge structure) are active, requiring stable power supply and suffering higher 1/*f* noise, while the ME sensor is driven with a magnetic bias and generates electric charge by itself, indicating that it is a passive two-terminal element, which can minimize the size of a ME measurement system without external batteries and achieve a low-power consumption. Moreover, an array of the ME sensors can be built up and placed closer to the muscle of interest owing

to their small dimension. Thus, the miniaturised ME sensor could be an effective alternative for future MMG measurements with relatively low operating costs.

In this paper, a finite-size trilayer ME laminate structures is designed and optimized using *COMSOL Multiphysics*, a commercial finite-element method (FEM) software. A general physical concept of the ME sensor is presented. In addition, the mathematical models are presented with numerical simulations setup including governing equations, constitutive relations, and boundary conditions. Furthermore, the FEM simulation results are compared with experimental results. An active geomagnetic field cancellation system is also developed to test fabricated ME sensors with its readout circuitry to achieve on-chip signal processing and noise cancellation [29].

II. Magnetoelectric Methodology

A. Magnetoelectric Effect

The ME effect is a special phenomenon in which the electric polarization can be generated by a changing magnetic field. It is a result of the product of a magnetostrictive (MS) effect in the magnetic phase and a piezoelectric (PE) effect in the PE phase. Then, the ME voltage coefficient, α_{ME}, can be expressed as [19], [30]:

$$\alpha_{\mathrm{ME}} = \frac{\mathrm{Mechanical}}{\mathrm{Magnetic}} \times \frac{\mathrm{Electric}}{\mathrm{Mechanical}} = \frac{\partial \epsilon}{\partial \mathrm{H}} \times \frac{\partial \sigma}{\partial \epsilon} \times \frac{\partial \mathrm{P}}{\partial \sigma} \tag{1}$$

which depends upon the materials combination, interface quality, DC magnetic bias, and operational mode [18], [31].

Applying a magnetic field, H, along the length direction of the ME composite, the MS layer will elongate along the field direction and generate a strain tensor, ϵ, by magnetostriction, which will transfer a stress tensor, σ, to the PE layer, where the polarization, P, is changed with stress. Therefore, there is a potential difference induced along the thickness direction of the PE layer due to the transverse response. In order to enhance this response and improve the sensor sensitivity, a low harmonic magnetic field is commonly employed using an exciting coil surrounding the sensor operated at a mechanical resonance frequency [32]. Thus, the thin-film ME sensors can transform magnetic fields into a measurable polarization via a mechanical coupling of the MS and PE layers. Such strong ME coupling provides greater flexibility for applications as biosensing devices. Since the one-end of the sensor is fixed, for cantilever ME sensors with length $\gg$ width $\gg$ height, it only has one sensitivity direction to avoid a cross-sensitivity problem. It is noted that assembled sensor arrays are a common method utilized for the vector measurements. State-of-the-art magnetic field sensors based on thin-film ME composites have demonstrated their potential of sub-pT fields detection at room temperature under certain conditions [16], [23], [33]–[36] and with an extremely low magnetic noise level [22]. Still, it is difficult to predict how precisely a sensor behaves when an external magnetic field is applied, especially when the sensor structure comprises several layers of materials. Testing all combinations of structures and materials in the fabrication is expensive and time-consuming. Instead, accurate and reliable simulation techniques can help to evaluate the behaviours of certain material combinations and sensor geometries.

B. Simulation Procedures

The main challenge in FEM simulation is to accurately analyse the coupling of electric, magnetic, and mechanical fields between MS and PE layers during the response of the ME sensor. To overcome this problem, these three coupled fields can be computed in two steps, as illustrated in Fig. 2(a). Firstly, *a static finite-element (FE) problem* is analysed, allowing the calculation of the coefficients to build the constitutive law of the MS phase [37]. The corresponding initial condition is without applied stress and the magnetic induction is produced due to the presence of the static magnetic field. The constant DC magnetic field driven by the coils should be accurately computed and the key variable is the uniform magnetic potential on the ME sensor. Secondly, *a harmonic FE problem* is discussed to solve the electric potential by applying a harmonic magnetic field at a resonance state.

We investigated the suitability of three-dimensional (3D) FEM simulations to model the quasi-static bending-mode response of cantilever ME sensors. Traditionally, 3D physical models are studied separately in FEM software and then simulation results will be sent to a signal flow IC system model with a fixed configuration. This approach will bring about that any change in the configuration requires an extra round of FEM simulations. Therefore, a barrier is formed between the physical model and the integrated circuit system model (see Fig. 2(b)). To avoid this situation, an ME sensor compact model is developed. Here, a FEM model of the ME sensor is created and simulated in *COMSOL*. The parameters of the FEM model were then exported into *Cadence* using *Verilog-A* language, which connects both models for integrated chip designers.

The dynamic small-signal principle of the ME sensor is demonstrated in Fig. 2(c). A linear response with the largest sensitivity can be obtained around a proper DC bias point. The α_{ME} and the resonance frequency are evaluated regarding the operation point obtained in the nonlinear static FEM analysis.

C. Simulation Model Blocks

The common structures of the thin-film based ME sensor are illustrated in [35], [38], [39]. Compared with previous bulk laminate structures [40]–[42], they are compatible with microelectronic processes without epoxy bonding, enabling devices with better consistency and smaller size. The proposed ME sensor structure considering its fabrication is illustrated in Fig. 3(a). Here, we employed a laminated trilayer structure consisting of a PE layer sandwiched between a MS layer and a silicon layer. The compact FEM model is shown in Fig. 3(b) where all layers are assumed internal-stress-free at zero applied fields. The geometrical blocks are demonstrated below:

Airbox Block: The airbox provides a finite boundary and natural environment for the ME model where free space electric

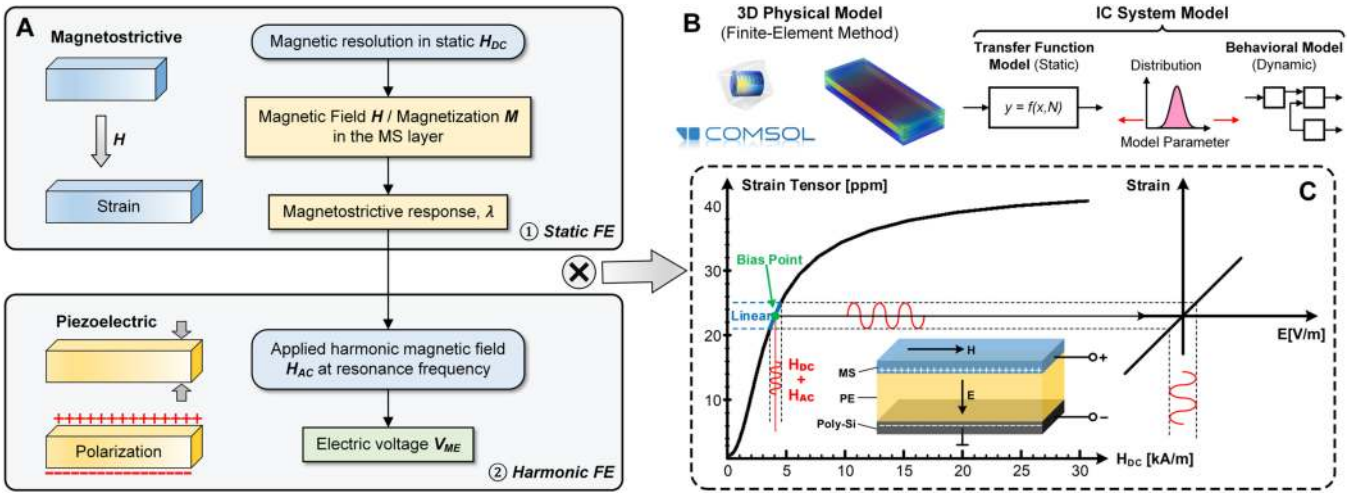

Fig. 2. (a) ME sensor modelling procedure; (b) Modelling silos between physical models and IC system models; and (c) Illustration of the dynamic small signal principle of the ME laminate with MS/PE/substrate structure.

and magnetic fields exist. This finite space area allows *COMSOL* to accurately resolve the FEM problems. Compared with the infinite environments, a time-consuming solution, it saves much computing time.

PE Block: The characteristics of the α_{ME} is governed by the choice of materials. Aluminium nitride (AlN), aluminium scandium nitride (AlScN), and lead zirconium titanate (PZT) are common PE materials for thin-film composites [43]. Although PZT ceramics favour a higher PE voltage coefficient, AlN has a much lower loss tangent and linear response to strain, which is preferable for this application.

MS Block & Poly-Si Block: The MS and Poly-Si blocks above and below the PE block form a ME laminate structure where an ideal contact between each layer is assumed. Here, the requirements for the MS layer depend on the piezomagnetic coefficient of the ferromagnetic material $d\lambda_{\mathrm{M}}/dH$, linked to the saturation magnetostriction, λ_{M}. Common high λ_{M} magnetic alloys are Terfenol-D ($Tb_{0.7}Dy_{0.3}Fe_2$), FeGa, $CoFe_2O_4$, and FeCo/TbFe multilayers, but they display relatively low permeabilities [19], [43]. Therefore, amorphous soft-magnetic alloys become better candidates with significantly high values of positive λ_{M} and high permeability. It is worth mentioning that the best known soft magnetic materials are $NiFe_2O_4$ and $CoFe_2O_4$ ferrites. Despite this, Terfenol-D with giant λ_{M} and Metglas (FeCoSiB) with the highest permeability are more widely used as a MS phase due to their high piezomagnetic coefficients. However, the Terfenol-D exhibits strong λ_{M} only under very large magnetic induction. In contrast, Metglas with a low saturation magnetic field thus very sensitive to ultra-low fields was chosen despite of a relatively poor λ_{M}.

Helmholtz Coil Block: A pair of circular Helmholtz coils are symmetrically located at both sides of the ME block where the current through the coils flows in the same direction. They are driven by adjustable bias currents to produce uniform AC and DC magnetic fields in the centre. In Fig. 3(b), the brown streamlines show the computed path of the coil currents.

D. Boundary Condition

In this model, all blocks are solved within an *AC/DC Magnetic Fields' Solver* of *COMSOL*. Subsequently, the trilayer ME sensor is resolved by *Structural Mechanics Solver.* This solver involves a magnetostrictive material function where a linear elastic material model is applied for the MS layer. The initial strain is defined from the magnetostriction of materials. Besides, a piezoelectric material function is involved for the AlN. In addition to mechanical and magnetic behaviour, it is essential to simulate an electrostatic behaviour of the sensor. Here, a *PZD Module* of *COMSOL* is employed for the MS and PE blocks and Helmholtz coil block, defined as electric materials. Regarding air-box boundaries, magnetic insulation and electric grounding are utilized on the surface. To easily calculate the ME voltage, the bottom layer is electrically grounded. Furthermore, the geometry symmetry is taken into account to reduce total computing time.

E. Mesh

The optimization of mesh distribution in FEM simulations can effectively improve accuracy and lower computation time, which are proportional to the mesh resolutions. The purpose of the selective meshing in the computed structure is to distribute mesh in more critical areas such as edges but less in secondary areas. In the proposed model, the order of decreasing fineness is divided into five levels of mesh resolutions as follows: 1) the ME laminate; 2) Helmholtz coils; 3) domain between the ME sensor and coils; 4) domain between coils and the airbox; 5) external air barrier.

F. Realization of the FEM Model

For variations of ultra-low magnetic fields, ME sensors are considered as a small signal behaviour at an optimized operating point. To resolve mechanical, magnetic and electric coupled fields, the following variables are computed following

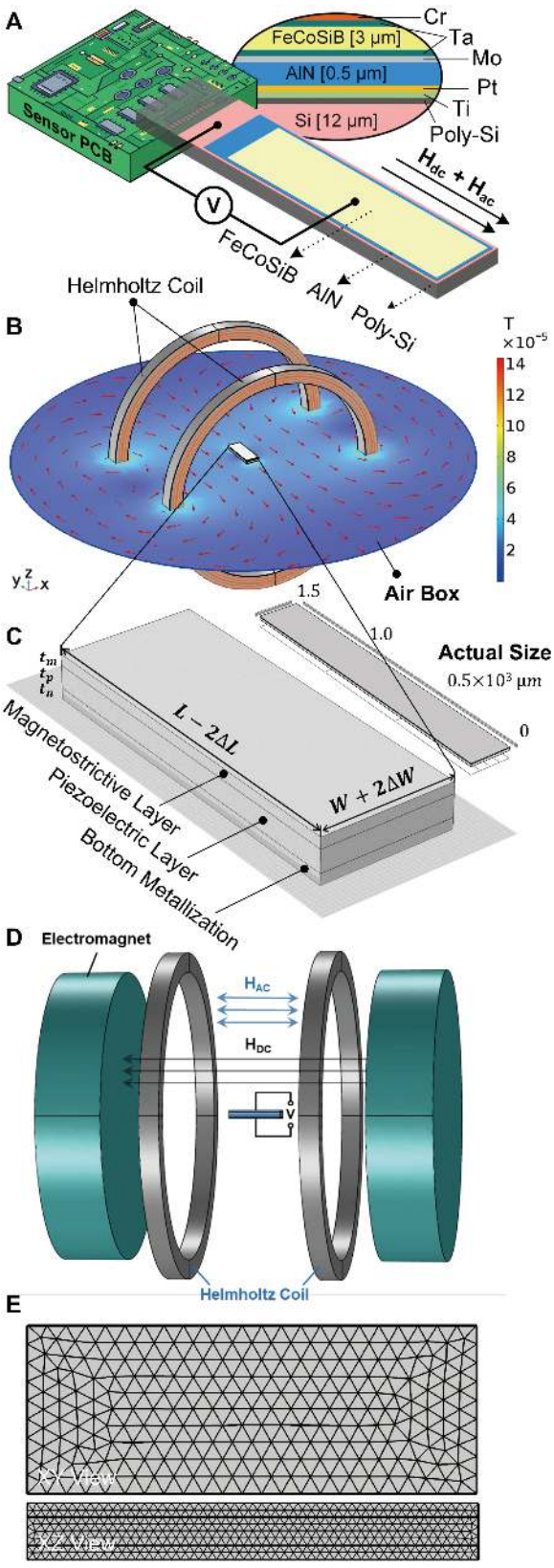

Fig. 3. (a) Schematic illustration of the fabricated ME sensor structure; (b) simulation result of uniform magnetic field distribution in the central x-y plane under the excitation of a pair of Helmholtz coils; (c) Enlarged ME structure; and (d) DC and AC magnetic field modelling, finding suitable bias DC magnetic field and the resonance frequency of the harmonic field to achieve the maximum α_{ME}. (e) Created Mesh from XY and XZ views.

a sequence: magnetization, normalized magnetic potential, mechanical displacement vector, electric polarization, and electric potential. The relationship of the electric field, $\boldsymbol{E}$, electric flux density, $\boldsymbol{D}$, magnetic field, $\boldsymbol{H}$, and magnetic flux density vectors, $\boldsymbol{B}$ are defined by the linear constitutive materials (2) to (4) [44], [45]:

$$\sigma_{ij} = c_{ijkl}\epsilon_{kl} - e_{kij}E_k - e^m_{kij}H_k \tag{2}$$

$$D_i = e_{ijk}\epsilon_{jk} + \kappa_{ij}E_j \tag{3}$$

$$B_i = e^m_{ijk}\varepsilon_{jk} + \mu_{ij}H_j \tag{4}$$

where σ and ϵ are the stress and strain tensors. c, e, e^m, κ, and μ are the stiffness, strain to electric field coupling constant, strain to magnetic field coupling constant, permittivity, and permeability. The geometry specification is shown in Fig. 3(c): $L = 1500\ \mu$m, $W = 200\ \mu$m, $t_{\mathrm{m}} = 6t_{\mathrm{p}} = 3\ \mu$m and $t_{\mathrm{n}} = 12\ \mu$m. The AlN and FeCoSiB are considered as PE and MS materials respectively, while the silicon substrate is modelled as isotropic material. The input parameters and used material properties are given in [46] and [47]. For a given layer, the constant material parameters and ideal interface lamination are assumed to prevent slippage of the layer during deformation. In addition, $e^m = 0$ for AlN and $e = 0$ for FeCoSiB are utilized since it is assumed that there is no inverse ME effect in used materials, and this means the piezoelectricity/magnetostriction in the MS/PE phases are neglected. Furthermore, a perfect conductive boundary condition is employed through the conductivity of the MS layer [45]. As a common approach, the stress attenuation along the layer thickness is negligible when calculating the α_{ME} [48]. The used materials' properties for simulations are summarized in the appendix, where parameters $\boldsymbol{c^{\mathrm{EH}}}$, $\boldsymbol{e}$, $\boldsymbol{e_{\mathrm{m}}}$, ϵ, $\boldsymbol{\mu}$, $\boldsymbol{\rho}$ and $\mathbf{tan}\boldsymbol{\delta}$ refer 4th order elastic matrix, stress-charge PE coupling matrix, strain to magnetic field coupling matrix, permittivity, permeability, density, and loss factor.

The calculation of ME sensor response is mainly performed with partial differential equations (PDEs) in which conduction currents and space charges are negligible. The electric field $\boldsymbol{E}$ and the magnetic field $\boldsymbol{H}$ can be expressed as $\boldsymbol{E} = -\nabla V$ and $\boldsymbol{H} = -\nabla V_{\mathrm{m}}$ in which V and V_{m} are scalar potentials. Then, five PDEs (5) to (7) are defined for the five variables u_1, u_2, u_3, V and V_{m} (with directions $x = 1$, $y = 2$ and $z = 3$):

$$\sigma_{ij,j} + f_i = \rho\ddot{u}_i \quad \text{with } i = 1, 2, 3 \tag{5}$$

$$\nabla \cdot \mathbf{D} = 0 \tag{6}$$

$$\nabla \cdot \mathbf{B} = 0 \tag{7}$$

where $\boldsymbol{u}$, ρ are the displacement vector and the charge density, while the polarization is related to the ρ as $\nabla \cdot \mathbf{P} = -\rho$. The strain components can be expressed as $\epsilon_{ij} = (u_{i,j} + u_{j,i})/2$.

The mentioned calculation is performed in the previously noted FEM software, *COMSOL Multiphysics*. More FEM simulation details are described in [45], [47], [49]. Coupled physical fields with a variety of geometries can be simultaneously calculated in different *COMSOL* modules. In this work, three different modules, *Magnetic Field Module*, *Solid Mechanics Module*, and *Electrostatics Module*, were used to obtain the static deformations. Based on the state-of-the-art analytical models

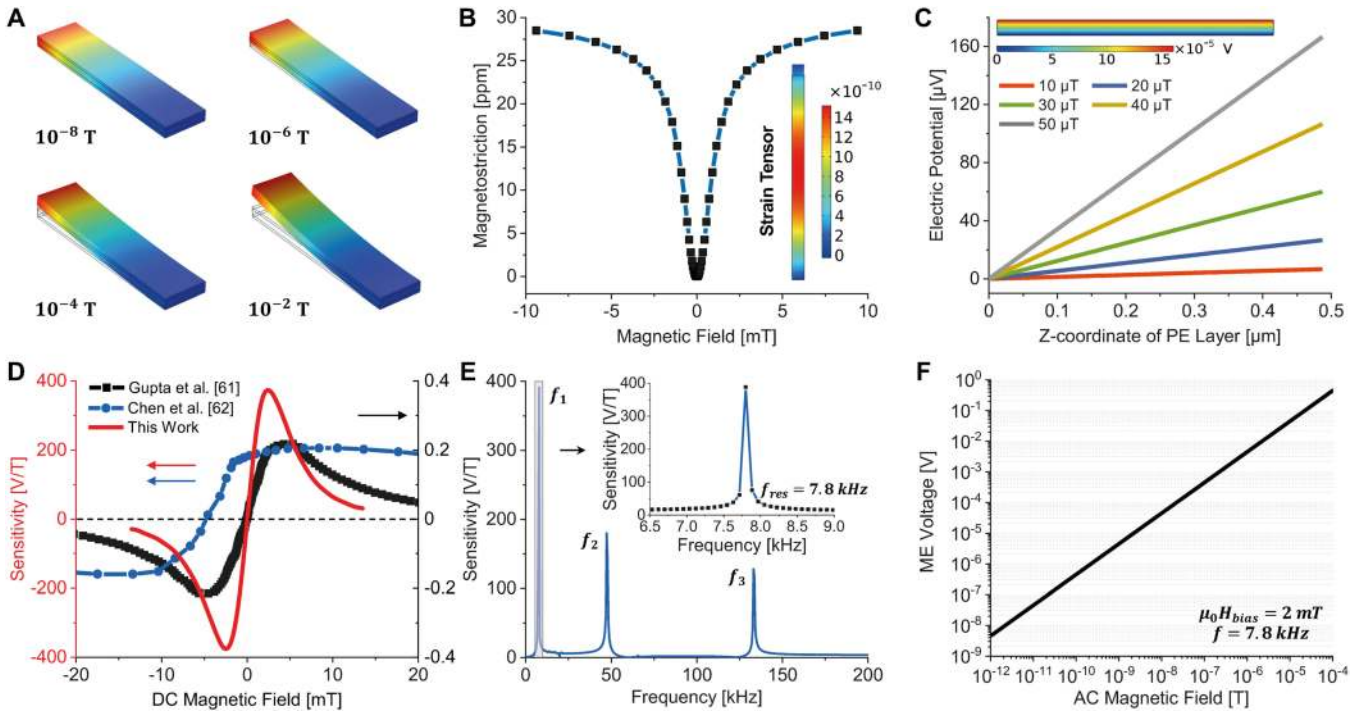

Fig. 4. (a) Computed displacements of the ME sensor with magnitudes of an external magnetic field from 10^{-8} to 10^{-2} T; (b) simulated magnetostriction curve for the magnetostrictive material; (c) ME voltage produced between top and bottom measurement points on the piezoelectric layer; (d) sensitivity of the longitudinal-transverse mode laminated ME sensor as a function of $H_{\rm DC}$, compared to state-of-the-art experimental outcomes; (e) frequency dependence of sensitivity, showing the resonance enhancement of ME interactions; and (f) ME voltage versus $H_{\rm AC}$ at the optimum working point ($H_{\rm Bias} = 2$ mT and $f_{\rm res} = 7.8$ kHz).

[50]–[53], three assumptions in these modules include (i) plane stress, (ii) overall homogeneous physical fields, and (iii) zero average stress at the laminate's facets. In addition, the measurement circuit condition [45], [54] is taken into account and magnetometric demagnetizing factor [55] is introduced. As mentioned previously, with accurate and optimized boundary conditions at the interfaces and facets of the ME sensor, *COMSOL* can resolve a series of numerical problems effectively. However, there is no built-in ME module directly in the software. The *Piezoelectric Devices Modules* consisting of a *Solid Mechanics Module* and an *Electrostatics Module* are adopted. Finally, the frequency-dependent ME voltages are evaluated through resolving eigenvalue problems and calculated by sweeping harmonic excitation frequencies appropriately to find the stationary solution.

In order to simulate the real environment of MMG signals. The Helmholtz coils and electromagnets are simultaneously implemented to provide a DC bias magnetic field and small AC field, as shown in Fig. 3(d). The ME voltage is calculated by measured voltage potentials along the thickness direction in the PE layer. Finally, the structure of the ME sensor was defined with different mesh resolutions. In other words, user-defined tetrahedral meshes divide a 3D structure into finite small elements to estimate the strain and polarization of the ME sensor by changing the strength of applied magnetic fields. Possible geometrical mismatches can be also considered. The computational meshes with different resolutions are shown in Fig. 3(e) with XY and XZ views of the ME sensor.

III. Modelling and Simulation Results

The overall computed displacements of the ME sensor from 10^{-8} to 10^{-2} T are demonstrated in Fig. 4(a). For a fixed right cantilever end, the strain generated from the MS layer will transfer to the PE layer and cause a bending effect, which depends on the magnitude of an external magnetic field. In order to accurately validate the ME response especially under the ultra-low magnetic field, the simulation results of each stage will be presented in detail as follows.

A. Magnetostriction Model in COMSOL

From the principle, the ME sensor is driven by a DC magnetic bias field to maximize the $\alpha_{\rm ME}$. That is because, in reality, the MS materials have a nonlinear response of strain or magnetostriction with applied magnetic fields and mechanical stress [56], [57]. Fig. 4(b) shows the modelled nonlinear response of used MS material, FeCoSiB, in which the colour legend indicates the strain in a single MS layer. The results are obtained from the parametric study that simulated a quasi-static rise of the current density in the Helmholtz coil. Here, the significantly nonlinear behaviour is shown in the region where the magnetic field $B_{\rm y}$ varies from 0 and 10 mT. This range with the sharpest strain change is very important for ME sensor modelling since the maximum $\alpha_{\rm ME}$ appears here [58]. The following parameters of the MS layer are adopted: saturation magnetization, 0.1 T and magnetostriction, 27∼30 ppm [59], validated from magnetometric and strain gauge measurements.

It is noted that the α_{ME} depends on the derivative of the magnetostriction curve. With color legend of generated strain tensor at a saturation state, the response curve is presented in Fig. 4(b), which is an even function and shows almost quadratic behaviour for the very low magnetic field. With an increase of the magnetic field, the operating point goes up and its slope is increased until reaching the maximum at a field of 2 mT in which a deflection point appears, and therefore having the steepest slope. In other words, small strength changes of the applied magnetic field around this operation point can lead to the largest variation in the MS material and thus to observe the largest α_{ME}.

B. Piezoelectric Material Modelling

For the piezoelectric material, AlN, the linear model is employed. The material properties are written with state-of-the-art constitutive relations in a strain-charge form [44]. Here, the MS and PE layers are assumed as a metal electrode and a perfect insulator respectively [46]. In addition, the upper FeCoSiB plate is electrically shielded outer circuits, which means there is zero net charge at the interface. The ME voltage is measured from a constant potential ϕ on this electrode, which totally depends on the $\boldsymbol{D}$ and $\boldsymbol{E}$ distributions. Furthermore, to resolve the electrostatic problem, the bottom silicon layer and the airbox with a finite area enclosed the entire structure are connected to the electric ground. Subsequently, generated ME voltages along the thickness of the PE layer is shown in Fig. 4(c) at different magnetic field strength from 10 μT to 50 μT.

C. Linear Transfer Curve of ME Sensor

For dynamic small AC magnetic field H_{AC}, an actual nonlinearity of the ME system can be solved linearly at a proper DC bias point since the amplitude of the measured MMG signals to be sensed are much lower than the bias magnetic field. The calculated α_{ME} of the longitudinal-transverse mode FeCoSiB/AlN/Si laminate as a function of the applied DC magnetic field H_{DC} is shown in Fig. 4(d). It indicate the α_{ME} strongly depends on the H_{DC}. At the beginning, the ME response curve is dramatically increased with weak magnetic fields, arriving a largest value, 382 V/T around 2 mT, which indicates that it reaches the maximum magnetostriction variation point. Subsequently, it is sharply decreased and finally vanished around 15 mT. The sensitivity curve matches very well with the fabrication results of the sandwiched composites [60], compared with state-of-the-art experimental outcomes [61], [62]. The simulation results are larger due to stress decay along with the layer thickness and the considered perfect mechanical coupling as well.

Due to mechanical coupling between the piezoelectric and magnetic phases, the performance of the ME sensor would be significantly enhanced if it is operated in a resonant state [63]–[65]. However, in a longitudinal mode, a main drawback of the ME effect at is that the frequency is quite high about a few hundred kHz. At such high frequencies, the eddy current losses in the MS phase will be very high, especially for transition metals and alloys, which brings about an inefficient ME energy conversion [66]. Therefore, one possible solution must be increasing the laminate size to reduce the operating frequency, but it is inconvenient for miniaturized systems for example wearable and implantable applications. Another alternative to achieve a stronger α_{ME} is applying a resonance frequency at a bending mode. It is expected that the frequency of the applied alternating magnetic field will be much lower compared to the longitudinal acoustic mode. Fig. 4(e) shows the frequency response of the ME sensor at the bending mode through resolving eigenvalue problems and sweeping harmonic excitation frequencies. The maximum sensitivity occurs at the 7.8 kHz frequency of bending oscillations and this peak value is almost 400 times higher than the low-frequency state.

The final setup is demonstrated as previous Fig. 3(c) where 2 mT DC bias field is driven from 15 mT magnetization of electromagnets while pico-Tesla range AC field (100 Hz) is generated by bias currents of the Helmholtz coils in the hundreds of nano-Amperes. The final induced voltages across the PE layer is shown in Fig. 4(f). The induced ME voltages have a perfectly linear relationship with applied magnetic field strength in the range from $\sim 10^{-12}$ T to $\sim 10^{-4}$ T. In other words, when the laminate is operated at resonance, the lowest detection ability is about 1 pT/$\sqrt{\mathrm{Hz}}$. In addition, it shows how small the ME voltage is changed with pico-Tesla magnetic fields, which unambiguously demonstrates that the ME sensor can offer high sensitivity to variations of the ultra-low fields.

To better analyse the overall performance from a system point of view and to prepare a custom tool for analogue circuit design, a *Verilog-A* compact model of the ME sensor is designed and optimized based on a physical aspect in FEM simulations. The ME device model can work as a voltage potential source as $V_{\mathrm{ME}} = S_V \cdot H_{\mathrm{AC}}$, where H_{AC} is the applied biomagnetic field strength ranging from -1 mT to $+1$ mT and the S_V is the sensitivity imported from *COMSOL*.

Furthermore, due to recorded mechanical vibrations of the ME sensors, there exists a challenging task that the desired signals are superimposed by unwanted signal components. To avoid this coupling effect and strengthen usability in real environments, further signal processing techniques should be employed. For examples, non-magnetic noise reference sensors can be utilized as adaptive noise cancellers and intelligent sensor readout techniques can be used. Moreover, improving low-frequency response has been widely explored over the past decades and common approaches are summarized in [66]. Therefore, future work is to achieve the same sensitivity at low frequencies of biomagnetic signals as at the resonance state using advanced signal processing techniques. This would further help to detect MMG signals below 100 Hz.

IV. Fabrication and Experimental Results

A. Measurement Setup

To reduce noise sources such as the acoustic noise and disturbances of magnetic and electric fields from the earth and surrounding equipment, the characterization of the ME sensor was operated in a shielded environment. In addition, an active compensation technique is employed to the whole system,

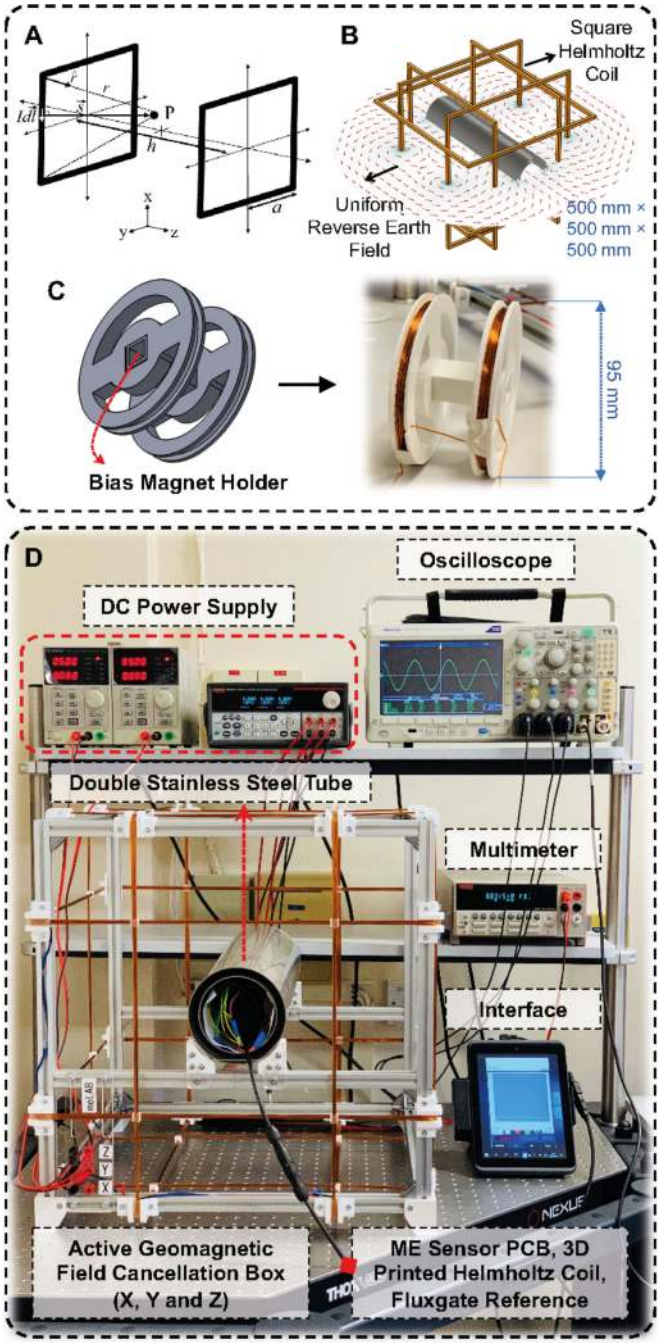

Fig. 5. Magnetic measurement setup: (a) working principle of square Helmholtz coils; (b) simulation results of uniform magnetic field distribution in the array of TSH coils; (c) 3D printed circular Helmholtz coil where two magnets are put on both sides of the coil to provide constant dc bias field; and (d) ME detection system with an active geomagnetic field cancellation box where double stainless steel tubes are in the middle.

mainly consisting an active geomagnetic field cancellation box with an array of tri-axial square Helmholtz (TSH) coils and a digital control unit. Three pairs are symmetrically located on *x*, *y*, *z* coordinate axis and operated with magnetic field compensation on each direction at the same time, which means the uniform reverse fields makes a dynamic equilibrium of the geomagnetic fields $B_{x,y,z} = 0$. The configuration is shown in Fig. 5(a) (in this

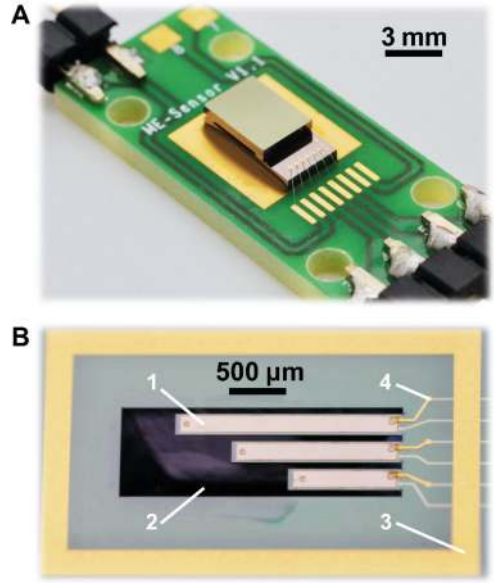

Fig. 6. ME sensor details: (a) image of the packaged and assembled ME chip on a test board (Fraunhofer Institute for Silicon Technology, Germany); (b) photograph of an uncapped ME sensor device with (1) ME cantilever, (2) etch groove, (3) bond frame, and (4) wire connecting to bond pads.

case *z*-axis). The governing equation for the magnetic field B at the centre point of a square coil pair is based on the Biot-Savart law [67], expressed as

$$d\vec{B} = \frac{\mu_0}{4\pi}\left(\frac{I\vec{dl}\times\hat{r}}{r^2}\right) \tag{8}$$

where μ_0 is the permeability of the free space, *I* is the driving current, *dl* is an infinitesimal segment of the current loop, *r* is the distance from an extreme of the current loop to the measurement point and $\hat{r}$ is a unit vector. In this square case, the two black square lines represent coils of conductive wires, consisting of *N* turns. Here, α is the half-side length of the coil, *P* is the measurement point. To achieve a homogeneous field at the centre point, the relationship between the side and the separation distance for square Helmholtz coils is given by a spacing ration of 0.5445 ($h = 1.089\alpha$) [68]. After solving (8) for $x = y = 0$, a highly uniform magnetic field can be generated by the square coils connected in series on the axis of symmetry, which is equal to the B_z component since the other (B_x and B_y) components are equal to zero and can be expressed as the equation (9). Besides, the dimension of the geomagnetic field cancellation box is designed for the applications of *in-vivo* and *in-vitro* biological systems. It allows performing experiments with small animals. The side length, *a*, is defined 500 mm on each symmetry axis *x*, *y* and *z* and the distance between two square coils are set as 270 mm.

To evaluate the distribution and uniformity of the magnetic field before fabricating the array of TSH coils, a compact finite-element model is designed in *COMSOL Multiphysics*. The environment is a sufficiently large airbox where the zero potential for electromagnetic analysis is operated using the AC/DC module and streamlines show the computed path of the coil currents.

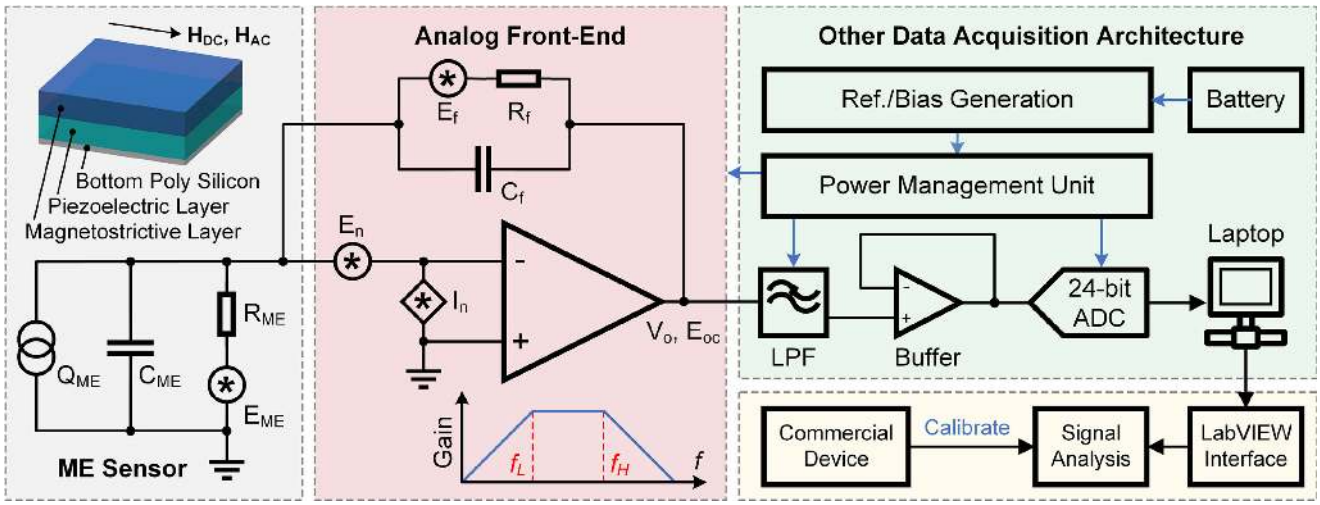

Fig. 7. Overview of ME detection system. The recorded signals by the ME sensor are performed by digitally controlled analog processing, which in general improves the readout of the sensor signals. The measured signals are passed to a digital signal enhancement stage, before a detailed analysis can be performed.

The specific conditions of TSH coils system with both physical and electrical parameters are taken into account: $N = 25$ turns and driving currents are set approximately to 1.2 A. Here, each pair of coils is energized independently and then generating a map of the magnetic flux density (B_x) shown in Fig. 5(b). The red arrows indicated the direction of the magnetic field lines and the uniformity region in the middle of whole system.

The magnets are utilized to provide a stable DC magnetic field which allows the ME sensor is performed in an optimum condition, but we need another coil to produce a small AC field. Both magnetic fields are aligned parallel to the long axis of the ME sensor. Here, a small 3D printed circular Helmholtz coil is designed and optimized to meet the size of stainless steel tubes, as shown in Fig. 5(c). The aim is to evaluate the ME sensor characteristics. Its principle is very similar to the square one. A pair of circular Helmholtz coils with the same direction of driven currents can generate a uniform region of the magnetic field. The ME sensor is then placed inside the coil with a pair of magnets located on both sides of the coil providing a stable bias magnetic field. The radius of two circular coils and the distance between each other have the same value. To generate pico-Tesla magnetic fields like MMG signals, precise and stable nano-ampere driving currents for copper coils are generated by LTC6082 from Linear Technology.

Finally, the experimental setup is shown in Fig. 5(d). The stainless steel tubes are also employed in the middle of the box to further shield the environmental magnetic field. The used equipment includes a triple channel DC power supply (2230-30-1) from KEITHLEY Tektronix, a stable DC power source (72-10500) from TENMA, a mixed domain oscilloscope (MDO3054), a digital precision multimeter (2000/E) from Tektronix. The results of the reference magnetometer, THM1176 from Metrolab Technology, Switzerland, is demonstrated in real-time on the screen interface based on LabVIEW. Both sensing systems were prepared and tested individually with a 24-bit 10 kSPS data acquisition system (EVAL-AD7177-2, Analog Devices, Inc).

During the experiment, the small variations of surrounding magnetic fields are mainly from the geomagnetic field, which is changing irregularly with time and has total magnitudes between 25 μT and 65 μT. After putting the sensor into the double stainless-steel tubes, the magnitude of magnetic noise dramatically decreased to almost zero ($\pm$100 nT). However, compared with the target, pico-Tesla biomagnetic fields, they are still relatively large. Fortunately, after utilizing the active geomagnetic field cancellation box, the in-plane magnetic field on the sensor surface can be sharply dropped to minimum of 4 nT, which can be ignored compared to 1.6 mT DC bias field.

B. *Fabrication of the ME Chip*

ME sensors were fabricated using surface micromachining process. Cantilevers were mounted on printed circuit boards (PCBs), and the top and bottom electrode connections were established manually. The packaged and assembled device on a test board is shown in Fig. 6(a). In the first step of the device wafer fabrication, a poly-silicon layer (12 μm) is deposited on 200 mm silicon wafer, isolated between two SiO_2 layers. Subsequently, Ti/Pt (as a bottom electrode), 0.5 μm AlN and Mo (as a top electrode) are deposited and patterned. In the next step, a front side deep reactive-ion etching is used to define the openings of the cavities. A thin passivation layer SiN_x (1 μm) is deposited and structured to the electrodes by dry etching. Afterwards, Au (4 μm) is electroplated as conductive wires, bond frames and contact pads using Ti/Au as plating base. After the magnetron sputter deposition and patterning in sequence of Ta/FeCoSiB (3 μm)/Ta/Cr (60 nm), microelectromechanical system ME resonators are finally released by anisotropic tetramethylammonium hydroxide etching of the Si substrate from the front side.

The cap wafer cavities are etched by the potassium hydroxide using a SiN_x layer as a hard mask. Followed by the removal of the hard mask, a SiO2 layer (650 nm) is grown on the cap wafer. In the next step, the bond frames with 4 μm Au and 3 μm Sn are

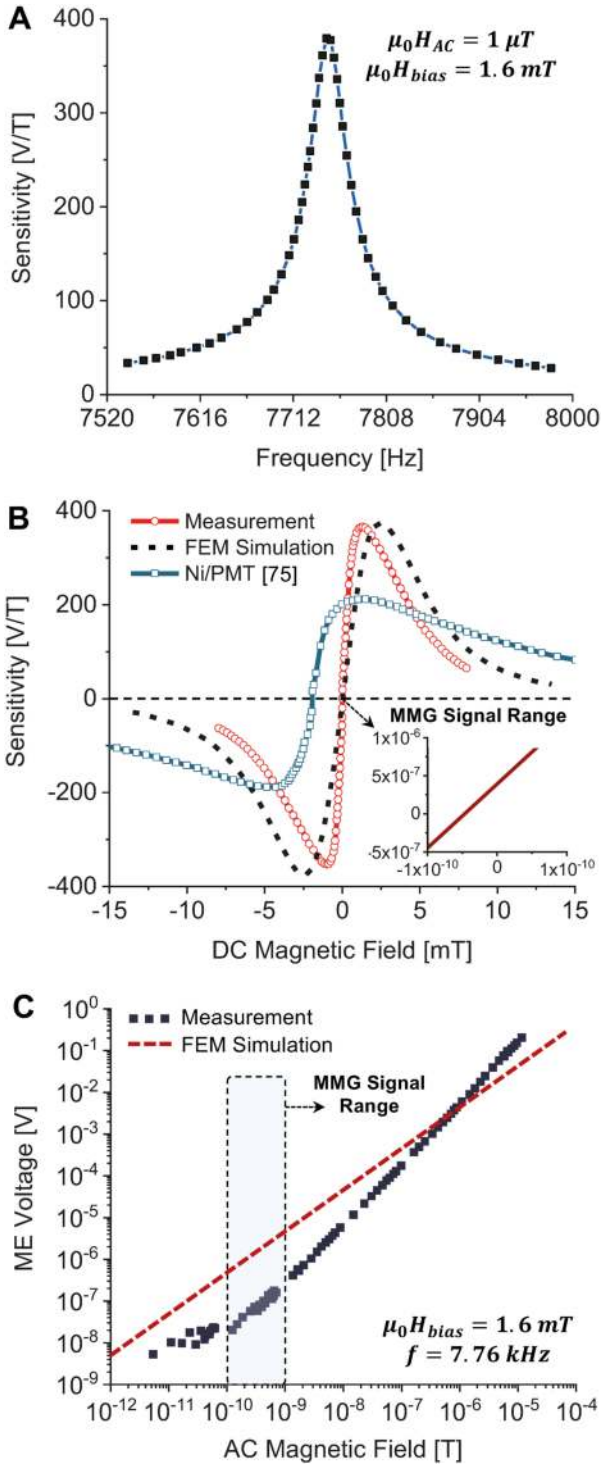

Fig. 8. (a) Frequency dependence of sensitivity; (b) measured sensitivity on the applied DC bias fields; and (c) AC sensitivity and linearity of the ME sensor.

electroplated using Ti/Au plating base. Ti getter material (400 nm) is deposited into the cap wafer cavities. After alignment, the device wafer and the cap wafer are brought into contact and bonded using Au/Sn transient liquid phase bonding process [69]. At the end, the vacuum encapsulated ME sensors are obtained after a dicing process. A photograph of a single nonencapsulated sensor is given in Fig. 6(b).

TABLE I
THE USED PARAMETERS FOR CALCULATION [73], [74]

Material	FeCoSiB	AlN	Poly-Si
Layer Thickness d [μm]	3	0.5	12
Young's Modulus [GPa]	176	288	160
Mass Density [g/cm^3]	7.25	3.30	2.33

To provide a stable DC bias field for ME sensors during the muscle movement, rather than the proposed 3D printed scheme of the cube magnet holder, our latest work is using integrated powder-based permanent magnets inside of the sensor chip to minimize the volume of the ME system [70].

$$\vec{B}(z) = \frac{2\mu_0 N I a^2}{\pi} \times \left[\left(a^2 + \left(z + \frac{h}{2} \right)^2 \right)^{-1} \left(2a^2 + \left(z + \frac{h}{2} \right)^2 \right)^{-0.5} + \left(a^2 + \left(z - \frac{h}{2} \right)^2 \right)^{-1} \left(2a^2 + \left(z - \frac{h}{2} \right)^2 \right)^{-0.5} \right] \tag{9}$$

C. Interface Circuitry

The miniaturized MMG system includes the ME sensor and the digital and analog electronic parts. A real-time readout system for newly developed ME sensors has been proposed and implemented. Fig. 7 shows functional blocks of system architecture, which comprises sensors, analog front-end (AFE), and digital back-end signal processing units. First of all, the equivalent circuit of the ME sensor and amplifier with the major internal noise source is shown. Due to its plate capacitor like structure, the capacitance C_{ME} dominates the circuit. The resistor R_{ME} contains resistive and polarization losses of the piezoelectric phase. Due to the low resistivity of the magnetostrictive and the metallization layer, those losses are not taken into account in the equivalent circuit. Here, two appropriate low noise preamplifiers with the low possible noise contribution meet the requirements of the high impedance of the ME sensor, which are charge and voltage amplifiers. However, previous work has shown that the former has a lower noise contribution than that of the latter [71]. Therefore, a charge amplifier setup using an Analog Devices AD745 is chosen to measure the sensor's linear response. The output voltage, V_{out}, of the charge amplifier depends on the charge Q_{ME} at its inverting input and the feedback capacitor C_f. Therefore, the ME voltage can be expressed as:

$$V_{out} = \frac{Q_{ME}}{C_f}, \quad V_{ME} = V_{out} \frac{C_f}{C_{ME}} \tag{10}$$

where C_f and C_{ME} should be chosen properly at the non-inverting amplifier input in order to resolve small sensor capacitance and additional noise from the charge amplifier. In addition, the feedback resistor, R_f, utilizing to bias the inverting input, can

TABLE II
COMPARISON OF STAT-OF-THE-ART MAGNETIC SENSORS FOR BIOMAGNETIC MEASUREMENTS

Magnetometer	Limit of Detection @ 1Hz	Limitations
SQUID Magnetometer	5 fT/√Hz @4.2K [78]	Cooling
Optically Pumped Atomic Magnetometers (Miniaturized)	700 fT√Hz [79]	Complex Setup, Heating
Giant Magnetoresistive Sensor	1 – 3.5 nT√Hz [80]	1/*f* noise, bias voltage/current
Magnetoelectric Sensors (This Work)	175 pT/√Hz	Sensor Size, bias magnetic fields

reduce the drift at the amplifier output. The low cut-off frequency and the gain of the charge amplifier, G_c, can be expressed as

$$f_{co} = \frac{1}{2 \cdot \pi \cdot R_f \cdot C_f}, \quad G_c = \frac{V_o}{V_{ME-oc}} = \frac{|Z_f|}{|Z_{ME}|} \tag{11}$$

where $C_f = 50$ pF and $R_f = 100$ MΩ are adopted at the output of the charge amplifier [71] where $Z_f = (R_f / (1 + j \cdot w \cdot C_f \cdot R_f)$ and $Z_{\rm ME} = (R_{\rm ME} / (1 + j{\cdot}w{\cdot}C_{\rm ME}{\cdot}R_{\rm ME})$. The $R_{\rm ME}$ contains resistive and polarization losses of the PE phase.

Due to a plate-capacitor-shaped structure, there is mainly one intrinsic noise source in the ME sensor, namely, the resistance of the PE phase, which leads to the thermal noise voltage $E_{\rm ME}$. Apart from that, there is also a thermal noise voltage E_f generated by R_f. Additionally, there exists noise contributions caused by the operational amplifier, which is represented by the noise voltage source $E_{\rm n}$ and the current noise source $I_{\rm n} = I_{\rm n+} = I_{\rm n-}$. The detail noise performance of resonant ME sensors is presented in [71].

In addition, the stable power supplies are provided by voltage regulators. Therefore, the proposed AFE includes a charge amplifier, bandpass filters, a programmable gain amplifier, an analog multiplexer, micro control unit, which includes an analog-to-digital converter. A power management unit with low-dropout regulators provides all required power supply voltages from a single 12V battery. Finally, the signals are transmitted to a laptop and then extracted, classified and displayed in a graphical user interface based on LabVIEW.

D. Measurement Results

Resonance Frequency: Fig. 8(a) illustrates the frequency dependence of the ME sensitivity. It is measured with a stable bias DC magnetic field of $\mu_0 H_{\rm bias} = 1.6$ mT and a low harmonic field of $\mu_0 H_{\rm ac} = 1$ μT. Here is a little bit different. To more accurately demonstrate the sensitivity, $S_{\rm V}$ and $\alpha_{\rm ME}$ to compare them with other works, the thickness of the piezoelectric layer $d_{\rm AlN}$ is added in the calculation, which can be expressed as

$$S_V = d_{AlN} \cdot \alpha_{ME} = d_{AlN} \cdot \frac{V_{ME}}{H_{AC}} \quad \left[\frac{V}{T}\right] \tag{12}$$

A static sensitivity of 18 V/T is obtained using the quality factor, $Q = 2217$, of the resonance curve when the ambient air pressure is zero. In addition, the ME response at a mechanical resonance state is observed. The maximum sensitivity is 378 V/T, obtained at the resonance frequency of 7.76 kHz. This is very consistent with the calculated value of 7.8 kHz in theory, which is the first resonance frequency by using the following equation [72]

$$f_r = \frac{1}{2\pi} \frac{\lambda_1^2}{L^2} \sqrt{\frac{\sum E_n I_n}{\sum m_n}} \tag{13}$$

where λ_1 is a constant 1.875 for a single side rigidly clamped rectangular cantilever beam; L is the length of the cantilever beam, E_n is Young's modulus, I_n is the moment of inertia and m_n is the mass per unit length of the individual layers of the material stack. Table I summarizes used parameters for the calculation [73], [74].

ME sensitivity: Fig. 8(b) shows the measured ME voltage in the response of external DC magnetic fields, compared with the simulation result and state-of-the-art fabrication outcome, Ni/PMT based ME sensors [75]. At a resonance state, the sensitivity of up to 378 V/T is observed by applying an optimum DC bias field of $\mu_0 H_{bias} = 1.6$ mT, which is basically matched with the simulation results. The used poly-Si instead of SiO_2 as substrate increased the Q. Moreover, an optimization of the thickness ratio between the MS and PE layers could lead to a higher $\alpha_{\rm ME}$ [16]. A vacuum environment at a wafer level for ME cantilever encapsulation in this work also enhanced the Q, which further enlarged the sensor sensitivity [76].

AC sensitivity and linearity: The sensitivity and linear response for AC signals is shown in Fig. 8(c). Except for relatively high fields of greater 1 μT, the sensor shows a linear response down to 175 pT. Below the data points, the measured ME voltages no longer depends on the applied magnetic field strength and are like scatters due to almost zero signal-to-noise ratio. It is well in the range of MMG signals from our finite-element modelling and experiments before [77]. To measure real MMG signals over a wide frequency band of 10 to 100 Hz without decreasing the noise level from the resonance state, the frequency conversion approach can be utilized. To remove additional noise introduced though this frequency conversion, on-chip magnetically shielding can be implemented in addition to bandpass filtering. Finally, Table II summarizes state-of-the-art sensors that have been utilized in MMG measurements with the detection limit at a 1 Hz magnetic signal and addresses their limitations [78]–[80].

V. CONCLUSION AND FUTURE WORK

In this paper, we demonstrated that pico-Tesla range signals can be measured with thin-film ME sensors at room temperature. A finite-size trilayer FeCoSiB/AlN/Si based ME laminate structure was designed, modelled and optimized in *COMSOL* FEM simulations and an active geomagnetic field cancellation

system was developed to test our fabricated ME sensor with its readout circuitry. With a 2 mT DC bias field, the sensitivity of 382V/T at a mechanical resonance frequency of 7.8 kHz was achieved. These outcomes are matched well with experimental results found in the literature and also our fabricated ME sensors. In the experiment, with an optimum bias field of 1.6 mT, measurements show that the sensor reaches a sensitivity of 378 V/T and low limit of detections of down to 175 pT/$\sqrt{}$Hz at a resonance frequency of 7.76 kHz. Compared to bulk composite ME sensors, the proposed thin-film based sensor has smaller size without sacrificing its sensitivity and thus offers better performance in the spatial resolution. Benefiting from complementary information of the magnetic field compared to electrical potential data, the miniaturized and economical ME sensor makes it an efficient and robust alternative to medical diagnosis and rehabilitation. Therefore, it is expected that this targeted, repeatable and safe sensor system could be suitable for future biomagnetic measurement in MMG systems. Future implementations without arm-sized shields will enable real-time geomagnetic field cancelling and furthering research is towards better understanding and diagnoses of movement disorders and motor neuron diseases.

Appendix
Material Property

Substrate: Polycrystalline Silicon (Poly-Si)

$$c_{Si}^{EH} = \begin{pmatrix} 216 & 84 & 84 & 0 & 0 & 0 \\ 84 & 216 & 84 & 0 & 0 & 0 \\ 84 & 84 & 216 & 0 & 0 & 0 \\ 0 & 0 & 0 & 66 & 0 & 0 \\ 0 & 0 & 0 & 0 & 66 & 0 \\ 0 & 0 & 0 & 0 & 0 & 66 \end{pmatrix} Gpa \quad \rho_{Si} = 2330 \text{ kg/m}^3$$

$$e_{Si} = \begin{pmatrix} 0 & 0 & 0 & 0 & 0 & 0 \\ 0 & 0 & 0 & 0 & 0 & 0 \\ 0 & 0 & 0 & 0 & 0 & 0 \end{pmatrix} N/Vm$$

$$\epsilon_{Si} = \begin{pmatrix} 107 & 0 & 0 \\ 0 & 107 & 0 \\ 0 & 0 & 107 \end{pmatrix} pF/m$$

$$e_{m,Si} = \begin{pmatrix} 0 & 0 & 0 & 0 & 0 & 0 \\ 0 & 0 & 0 & 0 & 0 & 0 \\ 0 & 0 & 0 & 0 & 0 & 0 \end{pmatrix} N/Am$$

$$\mu_{Si} = \begin{pmatrix} 0.4\pi & 0 & 0 \\ 0 & 0.4\pi & 0 \\ 0 & 0 & 0.4\pi \end{pmatrix} \mu H/m$$

Piezoelectric Material: Aluminium Nitride (AlN)

$$c_{AlN}^{EH} = \begin{pmatrix} 410 & 149 & 99 & 0 & 0 & 0 \\ 149 & 410 & 99 & 0 & 0 & 0 \\ 99 & 99 & 389 & 0 & 0 & 0 \\ 0 & 0 & 0 & 125 & 0 & 0 \\ 0 & 0 & 0 & 0 & 125 & 0 \\ 0 & 0 & 0 & 0 & 0 & 125 \end{pmatrix} Gpa$$

$$\rho_{PZT} = 3268\ kg/m^3 \quad tan\delta_{PZT} = 0.001$$

$$e_{AlN} = \begin{pmatrix} 0 & 0 & 0 & 0 & -0.48 & 0 \\ 0 & 0 & 0 & -0.48 & 0 & 0 \\ -0.58 & -0.58 & 1.55 & 0 & 0 & 0 \end{pmatrix} N/Vm$$

$$\epsilon_{AlN} = \begin{pmatrix} 80 & 0 & 0 \\ 0 & 80 & 0 \\ 0 & 0 & 80 \end{pmatrix} pF/m$$

$$e_{m,AlN} = \begin{pmatrix} 0 & 0 & 0 & 0 & 0 & 0 \\ 0 & 0 & 0 & 0 & 0 & 0 \\ 0 & 0 & 0 & 0 & 0 & 0 \end{pmatrix} N/Am$$

$$\mu_{AlN} = \begin{pmatrix} 0.4\pi & 0 & 0 \\ 0 & 0.4\pi & 0 \\ 0 & 0 & 0.4\pi \end{pmatrix} \mu H/m$$

Magnetostrictive Material: Metglas (FeCoSiB)

$$c_{MG}^{EH} = \begin{pmatrix} 150 & 45 & 45 & 0 & 0 & 0 \\ 45 & 150 & 45 & 0 & 0 & 0 \\ 45 & 45 & 45 & 0 & 0 & 0 \\ 0 & 0 & 0 & 40 & 0 & 0 \\ 0 & 0 & 0 & 0 & 40 & 0 \\ 0 & 0 & 0 & 0 & 0 & 40 \end{pmatrix} Gpa$$

$$\rho_{MG} = 7250\ kg/m^3$$

$$e_{MG} = \begin{pmatrix} 0 & 0 & 0 & 0 & 0 & 0 \\ 0 & 0 & 0 & 0 & 0 & 0 \\ 0 & 0 & 0 & 0 & 0 & 0 \end{pmatrix} N/Vm$$

$$\epsilon_{MG} = \begin{pmatrix} 8854 & 0 & 0 \\ 0 & 8854 & 0 \\ 0 & 0 & 8854 \end{pmatrix} pF/m$$

$$e_{m,MG} = \begin{pmatrix} 8500 & -2833.3 & -2833.3 & 0 & 0 & 0 \\ 0 & 0 & 0 & 0 & 0 & 0 \\ 0 & 0 & 0 & 0 & 0 & 0 \end{pmatrix} N/Am$$

$$\mu_{MG} = \begin{pmatrix} 1131 & 0 & 0 \\ 0 & 1131 & 0 \\ 0 & 0 & 1131 \end{pmatrix} \mu H/m$$

Environment: Air

$$\epsilon_{Air} = \begin{pmatrix} 8854 & 0 & 0 \\ 0 & 8854 & 0 \\ 0 & 0 & 8854 \end{pmatrix} pF/m$$

$$\mu_{Air} = \begin{pmatrix} 0.4\pi & 0 & 0 \\ 0 & 0.4\pi & 0 \\ 0 & 0 & 0.4\pi \end{pmatrix} \mu H/m$$

Acknowledgment

The authors would like to thank the German Research Foundation who funded this work through the CRC 1261.

References

[1] R. Merletti and P. A. Parker, *Electromyography: Physiology, Engineering, and Non-Invasive Applications*, vol. 11. Hoboken, NJ, USA: John Wiley & Sons, 2004.

[2] D. Cohen and E. Givler, "Magnetomyography: Magnetic fields around the human body produced by skeletal muscles," *Appl. Phys. Lett.*, vol. 21, no. 3, pp. 114–116, 1972.

[3] K. K. Parker and J. P. Wikswo, "A model of the magnetic fields created by single motor unit compound action potentials in skeletal muscle," *IEEE Trans. Biomed. Eng.*, vol. 44, no. 10, pp. 948–957, Oct. 1997.

[4] M. A. C. C. Garcia and O. Baffa, "Magnetic fields from skeletal muscles: A valuable physiological measurement?" *Front. Physiol.*, vol. 6, no. Aug., pp. 1–4, 2015.

[5] K. Woeppel, Q. Yang, and X. T. Cui, "Recent advances in neural electrode–tissue interfaces," *Curr. Opin. Biomed. Eng.*, vol. 4, pp. 21–31, 2017.

[6] J. Malmivuo and R. Plonsey, *Bioelectromagnetism: Principles and Applications of Bioelectric and Biomagnetic Fields*. USA: Oxford University Press, 1995.

[7] M. N. Ustinin *et al.*, "Reconstruction of the human hand functional structure based on a magnetomyogram," *Mat. Biol. i Bioinformatika*, vol. 13, no. 2, pp. 480–489, 2018.

[8] P. J. Broser *et al.*, "Optically pumped magnetometers for magnetomyography to study the innervation of the hand," *IEEE Trans. Neural Syst. Rehabil. Eng.*, vol. 26, no. 11, pp. 2226–2230, Nov. 2018.

[9] G. Z. Iwata *et al.*, "Biomagnetic signals recorded during transcranial magnetic stimulation (TMS)-evoked peripheral muscular activity," 2019, *arXiv1909.11451*.

[10] E. Elzenheimer, H. Laufs, W. Schulte-Mattler, and G. Schmidt, "Magnetic measurement of electrically evoked muscle responses with optically pumped magnetometers," *IEEE Trans. Neural Syst. Rehabil. Eng.*, 2020.

[11] K. Sternickel and A. I. Braginski, "Biomagnetism using SQUIDs: Status and perspectives," *Supercond. Sci. Technol.*, vol. 19, no. 3, 2006, Art. no. S160.

[12] O. Alem *et al.*, "Fetal magnetocardiography measurements with an array of microfabricated optically pumped magnetometers," *Phys. Med. Biol.*, vol. 60, no. 12, 2015, Art. no. 4797.

[13] E. Boto *et al.*, "A new generation of magnetoencephalography: Room temperature measurements using optically-pumped magnetometers," *Neuroimage*, vol. 149, pp. 404–414, 2017.

[14] H. Karo and I. Sasada, "Magnetocardiogram measured by fundamental mode orthogonal fluxgate array," *J. Appl. Phys.*, vol. 117, no. 17, 2015, Art. no. 17B322.

[15] S. Nakayama and T. Uchiyama, "Real-time measurement of biomagnetic vector fields in functional syncytium using amorphous metal," *Sci. Rep.*, vol. 5, pp. 1–9, 2015.

[16] S. Marauska, R. Jahns, H. Greve, E. Quandt, R. Knöchel, and B. Wagner, "MEMS magnetic field sensor based on magnetoelectric composites," *J. Micromech. Microeng.*, vol. 22, no. 6, 2012, Art. no. 65024.

[17] S. Marauska *et al.*, "Highly sensitive wafer-level packaged MEMS magnetic field sensor based on magnetoelectric composites," *Sensors Actuators A Phys.*, vol. 189, pp. 321–327, 2013.

[18] C.-W. Nan, M. I. Bichurin, S. Dong, D. Viehland, and G. Srinivasan, "Multiferroic magnetoelectric composites: Historical perspective, status, and future directions," *J. Appl. Phys.*, vol. 103, no. 3, 2008, Art. no. 031101.

[19] D. Viehland, M. Wuttig, J. McCord, and E. Quandt, "Magnetoelectric magnetic field sensors," *MRS Bull.*, vol. 43, no. 11, pp. 834–840, 2018.

[20] J. Reermann *et al.*, "Evaluation of magnetoelectric sensor systems for cardiological applications," *Meas.*, vol. 116, pp. 230–238, 2018.

[21] S. Salzer *et al.*, "Noise limits in thin-film magnetoelectric sensors with magnetic frequency conversion," *IEEE Sens. J.*, vol. 18, no. 2, pp. 596–604, Jan. 2018.

[22] A. Kittmann *et al.*, "Wide band low noise love wave magnetic field sensor system," *Sci. Rep.*, vol. 8, no. 1, pp. 278–287, 2018.

[23] V. Röbisch *et al.*, "Pushing the detection limit of thin film magnetoelectric heterostructures," *J. Mater. Res.*, vol. 32, no. 6, pp. 1009–1019, 2017.

[24] Y. Hui, T. Nan, N. X. Sun, and M. Rinaldi, "Ultra-sensitive magnetic field sensor based on a low-noise magnetoelectric MEMS-CMOS oscillator," in *Proc. IEEE Int. Freq. Control Symp.*, 2014, pp. 1–3.

[25] H. Heidari, S. Zuo, A. Krasoulis, and K. Nazarpour, "CMOS magnetic sensors for wearable magnetomyography," in *Proc. 40th Int. Conf. IEEE Eng. Med. Biol. Soc.*, 2018, pp. 2116–2119.

[26] H. Heidari, E. Bonizzoni, U. Gatti, and F. Maloberti, "A CMOS current-mode magnetic hall sensor with integrated front-end," *IEEE Trans. Circuits Syst. I Regul. Pap.*, vol. 62, no. 5, pp. 1270–1278, May 2015.

[27] P. P. Freitas, R. Ferreira, and S. Cardoso, "Spintronic Sensors," *Proc. IEEE*, vol. 104, no. 10, pp. 1894–1918, 2016.

[28] S. Zuo, K. Nazarpour and H. Heidari, "Device modeling of MgO-barrier tunneling magnetoresistors for hybrid spintronic-CMOS," *IEEE Electron Device Lett.*, vol. 39, no. 11, pp. 1784–1787, Nov. 2018.

[29] S. Zuo, H. Fan, K. Nazarpour, and H. Heidari, "A CMOS analog front-end for tunnelling magnetoresistive spintronic sensing systems," in *Proc. IEEE Int. Symp. Circuits Syst. (ISCAS)*, Sapporo, Japan, 2019, pp. 1–5.

[30] Y. Wang, J. Hu, Y. Lin, and C.-W. Nan, "Multiferroic magnetoelectric composite nanostructures," *NPG Asia Mater.*, vol. 2, no. 2, pp. 61–68, 2010.

[31] M. Bichurin and D. Viehland, *Magnetoelectricity in Composites*. Boca Raton, FL, USA: CRC Press, 2011.

[32] M. I. Bichurin, D. A. Filippov, V. M. Petrov, V. M. Laletsin, N. Paddubnaya, and G. Srinivasan, "Resonance magnetoelectric effects in layered magnetostrictive-piezoelectric composites," *Phys. Rev. B*, vol. 68, no. 13, 2003, Art. no. 132408.

[33] J. Zhai, Z. Xing, S. Dong, J. Li, and D. Viehland, "Detection of pico-Tesla magnetic fields using magneto-electric sensors at room temperature," *Appl. Phys. Lett.*, vol. 88, no. 6, 2006, Art. no. 62510.

[34] R. Jahns, R. Knochel, H. Greve, E. Woltermann, E. Lage, and E. Quandt, "Magnetoelectric sensors for biomagnetic measurements," in *Proc. MeMeA 2011 - 2011 IEEE Int. Symp. Med. Meas. Appl. Proc.*, 2011.

[35] R. Jahns *et al.*, "Giant magnetoelectric effect in thin-film composites," *J. Am. Ceram. Soc.*, vol. 96, no. 6, pp. 1673–1681, 2013.

[36] J. L. Gugat, M. C. Krantz, J. Schmalz, and M. Gerken, "Signal-to-noise ratio in cantilever magnetoelectric sensors," *IEEE Trans. Magn.*, vol. 52, no. 9, pp. 1–5, Sep. 2016.

[37] N. Galopin, X. Mininger, F. Frederic, and L. Daniel, "Finite element modeling of magnetoelectric sensors," *IEEE Trans. Magn.*, vol. 44, no. 6, pp. 834–837, Jun. 2008.

[38] A. Piorra *et al.*, "Magnetoelectric thin film composites with interdigital electrodes," *Appl. Phys. Lett.*, vol. 103, no. 3, 2013, Art. no. 32902.

[39] R. Zhang, G. Wu, and N. Zhang, "Magnetic force driven magnetoelectric effect in bi-cantilever composites," *AIP Adv.*, vol. 7, no. 12, 2017, Art. no. 125214.

[40] C. W. Nan, M. Li, and J. H. Huang, "Calculations of giant magnetoelectric effects in ferroic composites of rare-earth–iron alloys and ferroelectric polymers," *Phys. Rev. B*, vol. 63, no. 14, 2001, Art. no. 144415.

[41] J. Ryu, S. Priya, A. V. Carazo, K. Uchino, and H. Kim, "Effect of the magnetostrictive layer on magnetoelectric properties in lead zirconate titanate/terfenol-D laminate composites," *J. Am. Ceram. Soc.*, vol. 84, no. 12, pp. 2905–2908, 2001.

[42] S. Dong, J. Cheng, J. F. Li, and D. Viehland, "Enhanced magnetoelectric effects in laminate composites of Terfenol-D/Pb $(Zr,Ti)O_3$ under resonant drive," *Appl. Phys. Lett.*, vol. 83, no. 23, pp. 4812–4814, 2003.

[43] Z. Chu, M. PourhosseiniAsl, and S. Dong, "Review of multi-layered magnetoelectric composite materials and devices applications," *J. Phys. D. Appl. Phys.*, vol. 51, no. 24, 2018, Art. no. 243001.

[44] D. A. Berlincourt, D. R. Curran, and H. Jaffe, "Piezoelectric and piezomagnetic materials and their function in transducers," in *Physical Acoustics*, vol. 1. New York, NY, USA: Academic, pp. 169–270, 1964.

[45] J. F. Blackburn, M. Vopsaroiu, and M. G. Cain, "Verified finite element simulation of multiferroic structures: Solutions for conducting and insulating systems," *J. Appl. Phys.*, vol. 104, no. 7, 2008, Art. no. 74104.

[46] B. Zadov *et al.*, "Modeling of small DC magnetic field response in trilayer magnetoelectric laminate composites," *Adv. Condens. Matter Phys.*, vol. 2012, 2012, Art. no. 383728.

[47] J. L. Gugat, M. C. Krantz, and M. Gerken, "Two-dimensional versus three-dimensional finite-element method simulations of cantilever magnetoelectric sensors," *IEEE Trans. Magn.*, vol. 49, no. 10, pp. 5287–5293, Oct. 2013.

[48] L. Lin, Y. Wan, and F. Li, "An analytical nonlinear model for laminate multiferroic composites reproducing the DC magnetic bias dependent magnetoelectric properties," *IEEE Trans. Ultrason. Ferroelectr. Freq. Control*, vol. 59, no. 7, pp. 1568–1574, Jul. 2012.

[49] J. L. Gugat, J. Schmalz, M. C. Krantz, and M. Gerken, "Magnetic flux concentration effects in cantilever magnetoelectric sensors," *IEEE Trans. Magn.*, vol. 52, no. 5, pp. 1–8, May 2016.

[50] S. Priya, R. Islam, S. Dong, and D. Viehland, "Recent advancements in magnetoelectric particulate and laminate composites," *J. Electroceramics*, vol. 19, no. 1, pp. 149–166, 2007.

[51] G. Harshe, J. P. Dougherty, and R. E. Newnham, "Theoretical modelling of multilayer magnetoelectric composites," *Int. J. Appl. Electromagn. Mater.*, vol. 4, no. 2, p. 145, 1993.

[52] M. I. Bichurin, V. M. Petrov, and G. Srinivasan, "Theory of low-frequency magnetoelectric effects in ferromagnetic-ferroelectric layered composites," *J. Appl. Phys.*, vol. 92, no. 12, pp. 7681–7683, 2002.

[53] M. I. Bichurin, V. M. Petrov, and G. Srinivasan, "Theory of low-frequency magnetoelectric coupling in magnetostrictive-piezoelectric bilayers," *Phys. Rev. B*, vol. 68, no. 5, 2003, Art. no. 54402.

[54] E. Liverts, M. Auslender, A. Grosz, B. Zadov, M. I. Bichurin, and E. Paperno, "Modeling of the magnetoelectric effect in finite-size three-layer laminates under closed-circuit conditions," *J. Appl. Phys.*, vol. 107, no. 9, 2010, Art. no. 09D914.

[55] E. Liverts *et al.*, "Demagnetizing factors for two parallel ferromagnetic plates and their applications to magnetoelectric laminated sensors," *J. Appl. Phys.*, vol. 109, no. 7, 2011, Art. no. 07D703.

[56] M. Li *et al.*, "Highly sensitive DC magnetic field sensor based on nonlinear ME effect," *IEEE sensors Lett*., vol. 1, no. 6, pp. 1–4, Dec. 2017.

[57] D. Burdin, D. Chashin, N. Ekonomov, L. Fetisov, Y. Fetisov, and M. Shamonin, "DC magnetic field sensing based on the nonlinear magnetoelectric effect in magnetic heterostructures," *J. Phys. D. Appl. Phys.*, vol. 49, no. 37, 2016, Art. no. 375002.

[58] F. C. Graham, C. Mudivarthi, S. Datta, and A. B. Flatau, "Modeling of a Galfenol transducer using the bidirectionally coupled magnetoelastic model," *Smart Mater. Struct.*, vol. 18, no. 10, 2009, Art. no. 104013.

[59] T. Lafont *et al.*, "Magnetostrictive–piezoelectric composite structures for energy harvesting," *J. Micromechanics Microengineering*, vol. 22, no. 9, 2012, Art. no. 94009.

[60] S. Dong and J. Zhai, "Equivalent circuit method for static and dynamic analysis of magnetoelectric laminated composites," *Chin. Sci. Bull.*, vol. 53, no. 14, pp. 2113–2123, 2008.

[61] R. Gupta *et al.*, "Giant magnetoelectric effect in PZT thin film deposited on nickel," *Energy Harvest. Syst.*, vol. 3, no. 2, pp. 181–188, 2016.

[62] L. Chen and Y. Wang, "Enhanced magnetic field sensitivity in magnetoelectric composite based on positive magnetostrictive/negative magnetostrictive/piezoelectric laminate heterostructure," *IEEE Trans. Magn.*, vol. 53, no. 11, pp. 1–5, Nov. 2017.

[63] J. G. Wan, Z. Y. Li, Y. Wang, M. Zeng, G. H. Wang, and J.-M. Liu, "Strong flexural resonant magnetoelectric effect in Terfenol-D/ epoxy-Pb $(Zr,Ti)O_3$ bilayer," *Appl. Phys. Lett.*, vol. 86, no. 20, 2005, Art. no. 202504.

[64] L. Li and X. M. Chen, "Magnetoelectric characteristics of a dual-mode magnetostrictive/piezoelectric bilayered composite," *Appl. Phys. Lett.*, vol. 92, no. 7, 2008, Art. no. 72903.

[65] J. Zhai, S. Dong, Z. Xing, J. Li, and D. Viehland, "Giant magnetoelectric effect in Metglas/polyvinylidene-fluoride laminates," *Appl. Phys. Lett.*, vol. 89, no. 8, 2006, Art. no. 83507.

[66] J. Ou-Yang *et al.*, "Magnetoelectric laminate composites: An overview of methods for improving the DC and low-frequency response," *J. Phys. D. Appl. Phys.*, vol. 51, no. 32, 2018, Art. no. 324005.

[67] P. T. Pappas, "The original ampere force and Biot-Savart and Lorentz forces," *Nuovo Cim. B*, vol. 76, no. 2, pp. 189–197, 1983.

[68] J. J. Abbott, "Parametric design of tri-axial nested Helmholtz coils," *Rev. Sci. Instrum.*, vol. 86, no. 5, 2015, Art. no. 54701.

[69] S. Marauska, M. Claus, T. Lisec, and B. Wagner, "Low temperature transient liquid phase bonding of Au/Sn and Cu/Sn electroplated material systems for MEMS wafer-level packaging," *Microsyst. Technol.*, vol. 19, no. 8, pp. 1119–1130, 2013.

[70] F. Niekiel *et al.*, 'Highly sensitive MEMS magnetic field sensors with integrated powder-based permanent magnets," *Sensors Actuators A Phys.*, vol. 297, 2019, Art. no. 111560.

[71] R. Jahns, H. Greve, E. Woltermann, E. Quandt, and R. H. Knochel, "Noise performance of magnetometers with resonant thin-film magnetoelectric sensors," *IEEE Trans. Instrum. Meas.*, vol. 60, no. 8, pp. 2995–3001, Aug. 2011.

[72] I. Voiculescu, M. E. Zaghloul, R. A. McGill, E. J. Houser, and G. K. Fedder, "Electrostatically actuated resonant microcantilever beam in CMOS technology for the detection of chemical weapons," *IEEE Sens. J.*, vol. 5, no. 4, pp. 641–647, Aug. 2005.

[73] H. Greve, E. Woltermann, H.-J. Quenzer, B. Wagner, and E. Quandt, "Giant magnetoelectric coefficients in (Fe 90 Co 10) 78 Si 12 B 10-AlN thin film composites," *Appl. Phys. Lett.*, vol. 96, no. 18, 2010, Art. no. 182501.

[74] J. F. Shackelford, Y.-H. Han, S. Kim, and S.-H. Kwon, *CRC Materials Sci. and Eng. Handbook*. Boca Raton, FL, USA: CRC press, 2016.

[75] Y. Zhou, S. Chul Yang, D. J. Apo, D. Maurya, and S. Priya, "Tunable self-biased magnetoelectric response in homogenous laminates," *Appl. Phys. Lett.*, vol. 101, no. 23, 2012, Art. no. 232905.

[76] B. Lee, S. Seok, and K. Chun, "A study on wafer level vacuum packaging for MEMS devices," *J. Micromech. Microeng.*, vol. 13, no. 5, pp. 663–669, 2003.

[77] S. Zuo, H. Heidari, D. Farina, and K. Nazarpour, "Miniaturized magnetic sensors for implantable magnetomyography," *Adv. Mater. Technol.*, 2020, Art. no. 2000185, doi: 10.1002/admt.202000185.

[78] M. Schmelz *et al.*, "Sub-fT/Hz1/2 resolution and field-stable SQUID magnetometer based on low parasitic capacitance sub-micrometer cross-type Josephson tunnel junctions," *Phys. C Supercond. its Appl.*, vol. 482, pp. 27–32, 2012.

[79] T. H. Sander, J. Preusser, R. Mhaskar, J. Kitching, L. Trahms, and S. Knappe, "Magnetoencephalography with a chip-scale atomic magnetometer," *Biomed. Opt. Exp.*, vol. 3, no. 5, pp. 981–990, 2012.

[80] F. Barbieri *et al.*, "Local recording of biological magnetic fields using giant magneto resistance-based micro-probes," *Sci. Rep.*, vol. 6, 2016, Art. no. 39330.